Journal of Wind Engineering & Industrial Aerodynamics 265 (2025) 106131

Contents lists available at ScienceDirect

Journal of Wind Engineering & Industrial Aerodynamics

journal homepage: www.elsevier.com/locate/jweia

LES study on inversion-capped atmospheric boundary layer flows over steep topography considering the effects of free-atmosphere lapse rate

Tong Zhou, Takeshi Ishihara *

Department of Civil Engineering, School of Engineering, The University of Tokyo, 113-8656, Japan

ARTICLE INFO

Keywords:
Large eddy simulation
Steep topography
Atmospheric boundary layer
Capping inversion
Free-atmosphere lapse rate
Atmospheric stratification

ABSTRACT

The capping temperature inversion is a common atmospheric phenomenon that strongly influences the mean flow and turbulence structures within the atmospheric boundary layer (ABL). In this study, full-scale large eddy simulations are utilized to shed light on the characteristics of inversion-capped ABL flows over steep hilly terrain. As atmospheric stratification increases, the vertical wind veer becomes stronger, creating asymmetric flow patterns in the hill wake, and the buoyancy force acts to resist turbulent wake motions. In contrast to the conventionally neutral boundary layer (CNBL) and the convective boundary layer (CBL) cases, the stable boundary layer (SBL) exhibits pronounced flow acceleration at the hilltop and a faster wake recovery on the lee side of the hill. Based on the quadrant analysis, flow separation and vortex shedding are found to enhance organized motions downstream of the hill crest. In the wake region, sweep and ejection motions are identified at different heights. Furthermore, a wind speed prediction approach is developed for inversion-capped ABL flows over steep hilly terrain under both stable and unstable stratifications. The proposed approach incorporates the effect of the free-atmosphere lapse rate. Overall, it shows satisfactory agreement in predicting mean wind speed profiles over steep hills under both CBL and SBL conditions. The overestimation of mean wind speed at the hilltop in the SBL case can be corrected using the σ coordinate transformation technique.

1. Introduction

To mitigate over-dependence on fossil fuels and address the associated environmental pollution, the wind energy industry continues to construct large-scale wind farms on complex terrains around the world. Compared to flat terrains, complex terrains pose greater challenges for the wind energy industry due to the intricate interactions between the atmospheric boundary layer (ABL) and the uneven terrains. Over the past few decades, significant efforts have been made to improve the understanding of flow physics over complex terrain through field measurements, wind tunnel experiments and computational fluid dynamics (CFD) simulations. Most previous investigations have revealed that the characteristics of flow over hilly terrains are strongly influenced by topographical features and atmospheric conditions.

With regards to topographical aspects, hill slope, hill shape and ground roughness have been identified as the primary factors influencing flow behavior over hills. The flow acceleration at the hill crest and the flow separation on the lee side increase significantly with increasing hill slope (Kobayashi et al., 1994; Ferreira et al., 1995; Kim et al., 1997, 2001; Neff and Meroney, 1998; Carpenter and Locke, 1999; Cao et al., 2012). Wake flow dynamics over gently sloping terrain are found to be sensitive to the wind shear and turbulence intensity of the oncoming flow (Ishihara et al., 2001; Yang et al., 2021; Li et al., 2024; Chen and Ishihara, 2025). In addition to the slope of terrain, the flow patterns and turbulent statistics around hills vary significantly with changes in the shape of terrain. In the case of three-dimensional (3-D) hills, the cavity zone is shorter due to the suppression of the 3-D wake (Ishihara et al., 2001). In contrast to the closed streamlines behind the 2-D ridges, the open streamlines on the lee side of the 3-D hill are attributed to the presence of spanwise flow (Ishihara and Hibi, 2002). Moreover, it was shown that the secondary recirculation region becomes thicker as the hill shape changes from 2-D to 3-D (Liu et al., 2020). Finally, ground roughness has a considerable effect on the turbulent flow fields over terrain. The speed-up factor at the hilltop is amplified in rough hills compared to that in smooth hills (Pearse et al., 1981; Ishihara and Hibi, 1998; Cao and Tamura, 2006, 2007). The recirculation bubble in the wake region of rough hills is enlarged since ground roughness accelerates flow separation (Ishihara et al., 2001; Takahashi et al., 2002;

---

* Corresponding author.
E-mail address: ishihara@bridge.t.u-tokyo.ac.jp (T. Ishihara).

https://doi.org/10.1016/j.jweia.2025.106131
Received 8 March 2025; Received in revised form 10 May 2025; Accepted 24 May 2025

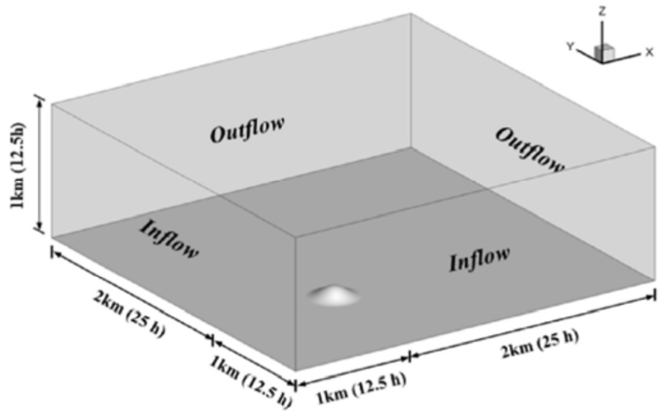

Fig. 1. Configuration of the computational domain.

Loureiro et al., 2008; Ishihara and Qi, 2019). Furthermore, the coupled effects of hill slope, hill shape and ground roughness need to be elucidated. It was demonstrated that the influence of ground roughness on the vertical profile of mean velocity over hilly terrain decreases with increasing hill slope (Liu et al., 2019). The similarity in the distributions of mean velocity and turbulence fluctuations between the 2-D ridge and the 3-D hill decreases as the hill slope increases (Liu et al., 2020).

Apart from topographical features, atmospheric conditions such as the Coriolis force and thermal stratification also play a crucial role in shaping turbulent flows over hills. Due to the vertical wind veer induced by the Coriolis force, turbulent vortices on the lee slope are deflected to one side, and the wake deflection becomes more pronounced as the horizontal scale of the mountain increases (Peng et al., 1995). Recently, Zhou and Ishihara (2023) conducted a quantitative evaluation of Coriolis effects on flow fields over hilly terrain. The results indicate that the Coriolis force has negligible effect on the speed-up ratio at the hill crest, but contributes to the velocity recovery in the hill wake. Another important factor is thermal stratification, which accounts for the buoyancy effect on the ABL flow. It was found that under stable stratification, both the wake depth and turbulent fluctuations over 2-D ridges are substantially reduced since negative buoyancy force suppresses the vertical fluid motions (Ross et al., 2004). The wake flow behind a 3-D hill remains attached to the ground surface due to the downward buoyancy force imposed by strong stable stratification (Chang et al., 2018; Uchida and Takakuwa, 2020). Moreover, it was shown that in the stable state, the maximum speed-up ratio at the hilltop decreases by about 40 % and the separation bubble elongates by about 10 % (Zhang et al., 2023). Furthermore, the combined effects of Coriolis force and thermal stratification on wake flows of hilly terrain were numerically investigated by Liu and Stevens (2021). It was revealed that the wake of a hill is strongly asymmetric in the stable boundary layer (SBL), whereas it is nearly symmetric in the convective boundary layer (CBL).

Despite considerable research on the influence of topographical factors and atmospheric conditions on turbulent flow fields over complex terrain, a research gap remains in that most prior studies overlook the effect of free-atmosphere lapse rate on atmospheric flows over

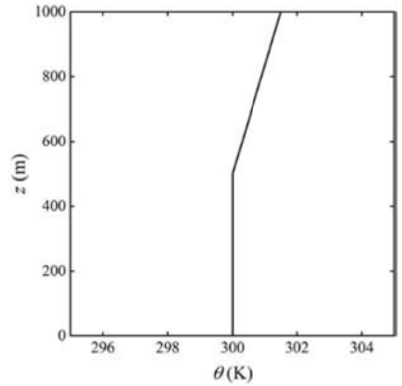

Fig. 3. Vertical profile of the initial potential temperature with a lapse rate of 3 K/km.

Table 1
Summary of numerical schemes and solution strategies.

Turbulence model	LES
SGS model	standard Smagorinsky model ($C_s = 0.1$)
Time discretization scheme	2nd order implicit backward scheme
Space discretization scheme	Convective term: 2nd order linear Diffusion term: 2nd order linear with non-orthogonal correction
Linear equation solvers	Velocity and temperature: PBiCG-DILU Pressure: PCG-GAMG
Time step size	0.1 s
Sampling duration	5400 s
Decoupling method	PIMPLE
Software	SOWFA (OpenFOAM-based flow solver)

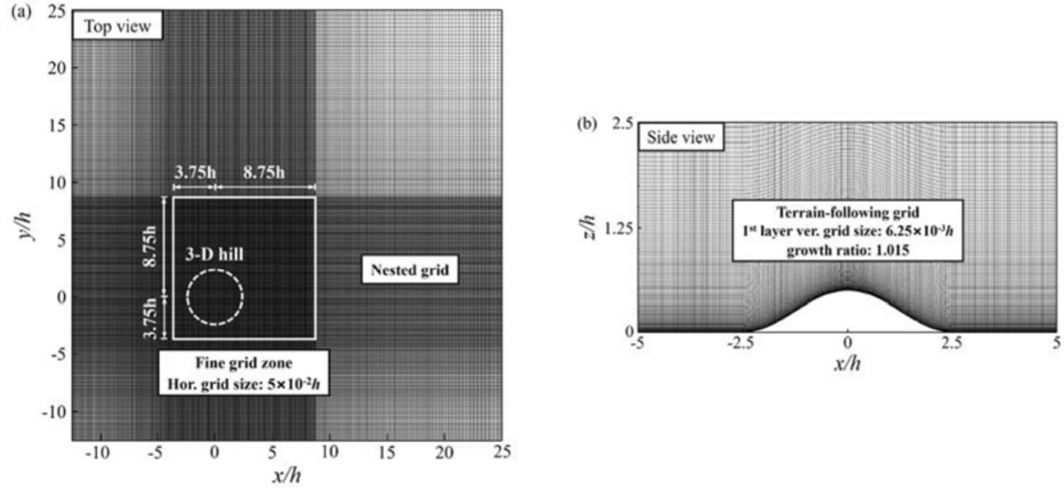

Fig. 2. Grid refinement strategies used in the successor simulations with the presence of steep topography: (a) nesting grid technique and (b) terrain-following grid technique.

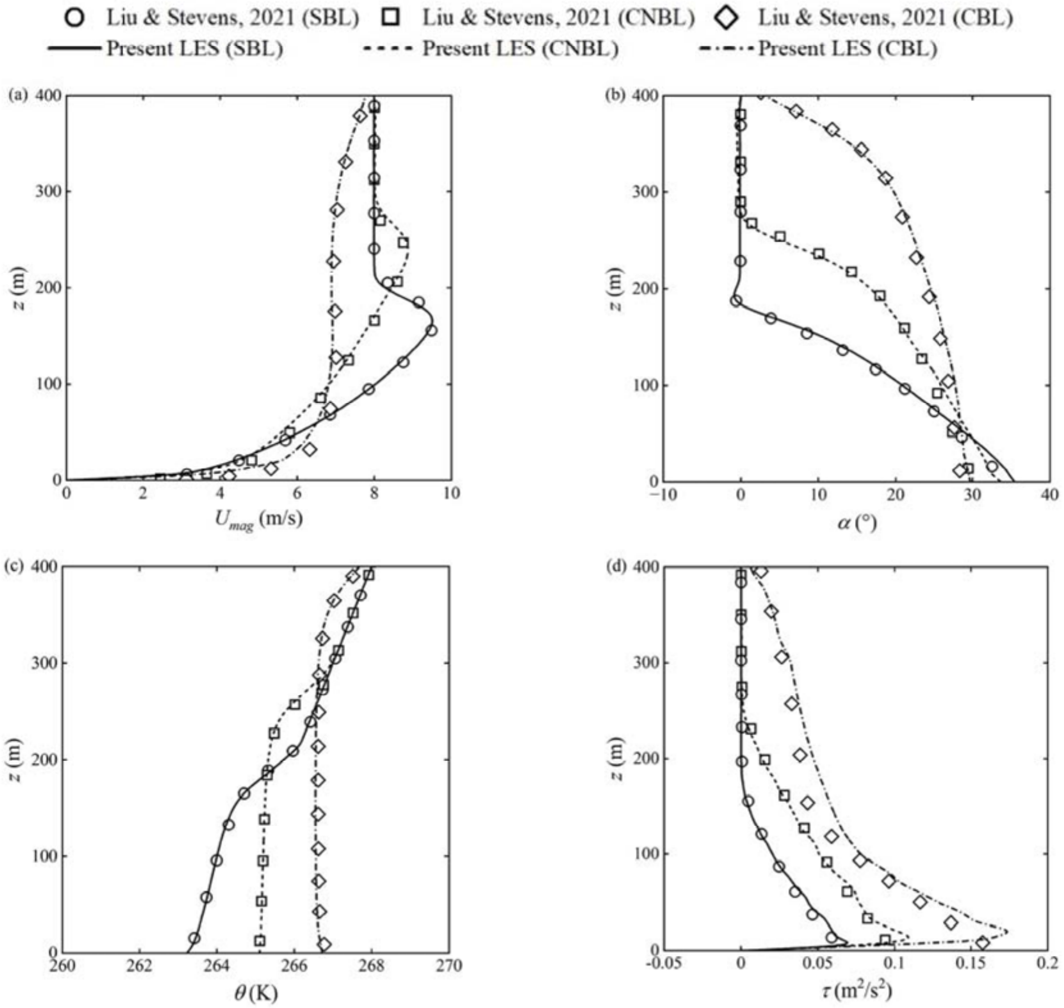

Fig. 4. Vertical profiles of stable, conventionally neutral and convective ABL flows over flat terrain: (a) mean wind speed, (b) mean wind direction, (c) mean potential temperature and (d) total turbulent momentum flux.

complex terrain. The free-atmosphere lapse rate is a widespread feature of the real atmosphere. It is worth noting that most neutrally stratified boundary layers are capped by stable stratification in the free atmosphere. This capping inversion reduces thermal entrainment from the free atmosphere, further reducing the boundary layer depth and the size of turbulent eddies. Moreover, turbulent vertical mixing and transport processes in the ABL are weakened by the free-atmosphere stratification. The second research gap lies in understanding the effects of the capping inversion on turbulent flows over complex terrain. Recently, the flow dynamics over steep hilly terrain under strong capping inversion were investigated by Liu and Stevens (2021). However, it should be mentioned that high inversion layer strength and low inversion layer height defined in their study may not adequately represent the atmospheric conditions in mid-latitude countries. Song et al. (2025) pointed out that the height of the capping inversion layer in Japan is generally higher than that in Northern Europe, resulting in a deeper boundary layer and stronger vertical mixing. Therefore, the interaction between atmospheric flow and complex terrain may vary significantly across countries located at different latitudes. The third research gap is the lack of a reliable approach for predicting mean wind speed over topography under thermally stratified ABL flows capped by an inversion layer. Although Zhou and Ishihara (2025) revealed that the effects of topography and atmospheric stability can be separated to predict the mean wind speed over hilly terrain under both stable and unstable stratification, the effects of free-atmosphere stratification in the real atmosphere have not been considered. It is crucial to further extend the generality of the analytical model in the context of inversion-capped ABL flows since it has practical implications for real engineering applications.

This study aims to (1) shed light on the characteristics of inversion-capped ABL flows with different atmospheric stability over a steep hill, (2) exhibit the effect of buoyancy force on flow acceleration at the hilltop and flow recovery on the lee side of hill in the convective and stable boundary layers, (3) provide a wind speed prediction approach for inversion-capped ABL flows over steep terrain under unstable and stable stratification. Section 2 presents the numerical model for simulating inversion-capped ABL flows over complex terrain by LES simulations. The numerical model in predicting thermally stratified atmospheric flows with an inversion-capped layer over flat terrain and the turbulent flow field over a 3-D steep hill is validated in Section 3. The effects of the free-atmosphere lapse rate on ABL flows over steep terrain are investigated and a wind speed prediction approach is proposed for inversion-capped ABL flows over steep terrain under unstable and stable stratification in Section 4. Finally, the main conclusions of the present study are briefly summarized in Section 5.

2. Numerical model

The simulation framework used in this study is explained in Section 2.1. The governing equations, computational domain and grid system are described in Sections 2.2 and 2.3. The boundary conditions,

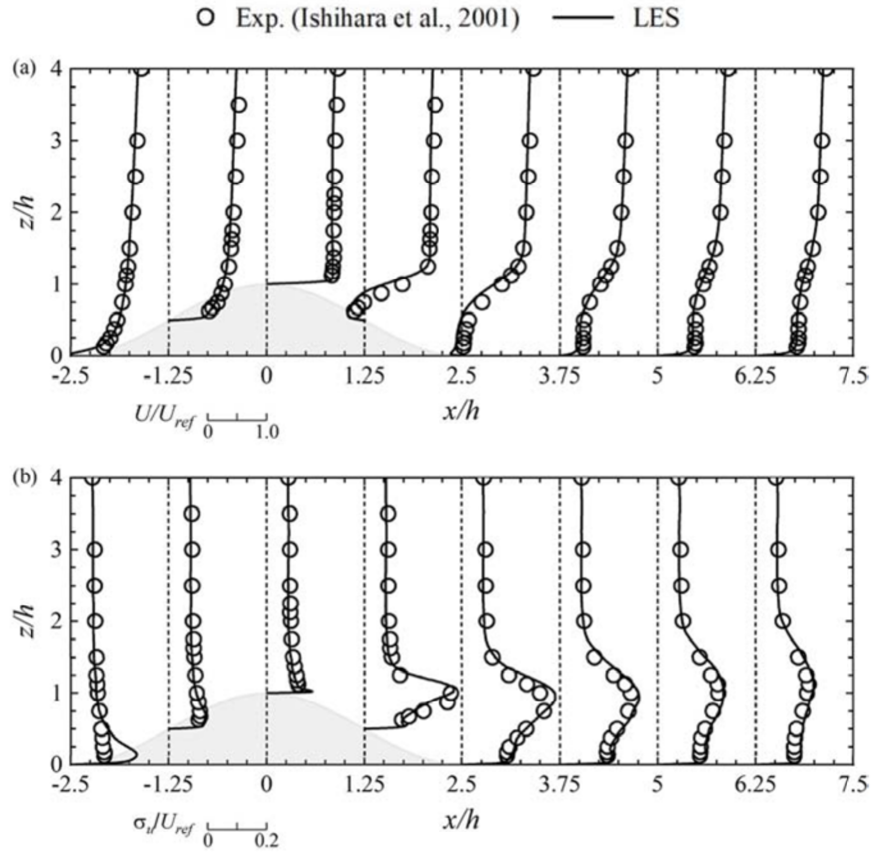

Fig. 5. Vertical profiles of turbulent statistics for turbulent flow fields over a steep hill: (a) mean velocity and (b) turbulence intensity.

numerical schemes and solution strategies are introduced in Sections 2.4 and 2.5.

2.1. Simulation framework

To simulate inversion-capped boundary layer flows over complex terrain under three typical atmospheric stability conditions, i.e., neutral, stable and unstable, numerical simulations are performed in two stages: a precursor ABL simulation and a successor terrain simulation.

In the first stage, thermally stratified ABL flows capped by a thermal inversion are reproduced in an empty computational domain, where the lateral boundaries are defined as periodic conditions to facilitate the development of horizontally uniform and statistically steady atmospheric flows at an affordable computational cost. The turbulent wind fields are driven by a constant pressure gradient based on a given geostrophic wind speed. Both the Coriolis force and atmospheric stability are incorporated into the numerical solver. Moreover, an initial capping inversion is established by prescribing an initial potential temperature profile. Furthermore, the ground roughness is modelled by adopting a wall shear stress model. Once the turbulent ABL flow field reaches a quasi-equilibrium state where the initial transient effects disappear, the flow variables such as velocity and potential temperature from the most upwind lateral boundaries are subsequently sampled by extending the computational time according to the requirements of the successor simulations.

For the second stage, the same numerical solver and computational domain are employed in the successor simulations to predict atmospheric flows over complex terrain. Instead of applying periodic boundary conditions on all lateral sides in the precursor domain, the space- and time-varying turbulence data (i.e., velocity and temperature) collected from the precursor simulations are fed into the successor simulations. Additionally, the downstream boundaries are specified as a zero-gradient outflow condition to ensure that the wake of the hill evolves smoothly without inducing artificial disturbance.

2.2. Governing equations

For the LES modelling of inversion-capped ABL flows under various thermal stratifications, the time-dependent incompressible Navier-Stokes equations are resolved after the spatial filtering procedure. The buoyancy effects associated with thermal stratification are modelled using the Bossiness approximation as shown in Churchfield et al. (2012). Hence, the governing equations including the continuity, momentum and energy conservation equations can be expressed as follows:

$$\frac{\partial \overline{u}_i}{\partial x_i}=0 \tag{1}$$

$$\frac{\partial \overline{u}_i}{\partial t}+\frac{\partial(\overline{u}_i\overline{u}_j)}{\partial x_j}=-\frac{\partial \widetilde{p}}{\partial x_i}-\frac{1}{\rho_0}\frac{\partial}{\partial x_i}p_0(x,y)-\frac{\partial \tau_{ij}}{\partial x_j}+g\left(\frac{\overline{\theta}-\theta_0}{\theta_0}\right)\delta_{i3}-2\epsilon_{ijk}\Omega_j\overline{u}_k \tag{2}$$

$$\frac{\partial \overline{\theta}}{\partial t}+\frac{\partial(\overline{u}_j\overline{\theta})}{\partial x_j}=-\frac{\partial \tau_{\theta j}}{\partial x_j} \tag{3}$$

where the overbar stands for the spatial filtering operation, $u_i=(u,v,w)$ denotes the resolved-scale velocity components, $x_i=(x,y,z)$ represents the spatial coordinates in three orthogonal directions, i.e., streamwise, spanwise and vertical directions, $\widetilde{p}$ is the density-normalized pressure, $p_0(x,y)$ is the horizontal-mean driving pressure, ρ_0 is the air density ($\rho_0 = 1.225\ \mathrm{kg\ m^{-3}}$), the gravitational acceleration g is taken to be $9.81\ \mathrm{ms^{-2}}$, $\overline{\theta}$ is the resolved-scale potential temperature, $\theta_0=300\ \mathrm{K}$ is used as a reference potential temperature, δ_{ij} is the Kronecker delta, ϵ_{ijk} is the alternating tensor and $\Omega_j=(0,\omega\, cos(\phi),\omega \sin(\phi))$ is the rotation

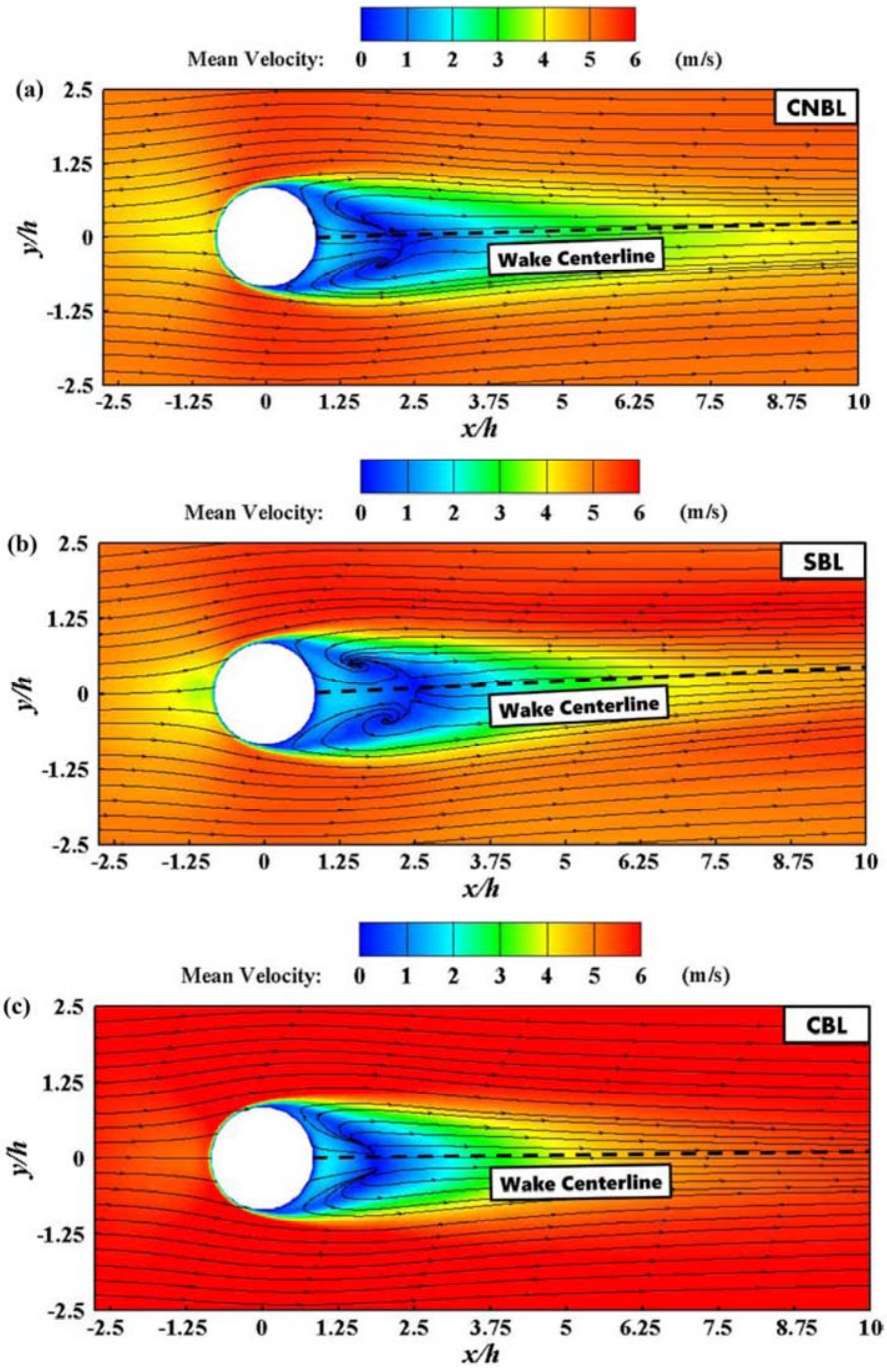

Fig. 6. Contours and streamlines of mean velocity on the horizontal plane of $z/h = 3/4$ for inversion-capped ABL flows over a steep hill: (a) CNBL, (b) SBL and (c) CBL.

rate vector. In this study, the planetary rotation rate is set to $\omega = 7.27 \times 10^{-5}$ rad s^{-1} and the latitude ϕ is determined to be 36°N (corresponding to the location of Tokyo, Japan). To consider the effects of unresolved-scale eddy motions on the resolved-scale flow field, the subgrid-scale (SGS) stress τ_{ij} and the SGS temperature flux $\tau_{\theta j}$ are defined as:

$$\tau_{ij} = -2\nu_t \overline{S}_{ij} + \frac{1}{3}\tau_{kk}\delta_{ij} \tag{4}$$

$$\tau_{\theta j} = -\frac{\upsilon_t}{Pr_t}\frac{\partial \overline{\theta}}{\partial x_j} \tag{5}$$

where υ_t is the SGS eddy viscosity, $\overline{S}_{ij}$ is the symmetric part of the resolved velocity gradient tensor and Pr_t is the turbulent Prandtl number.

In the above relations of Eq. (4) and Eq. (5), the SGS eddy viscosity and the turbulent Prandtl number should be prescribed, respectively. The standard Smagorinsky model is employed to parameterize the SGS eddy viscosity as follows:

$$\nu_t = (C_s\overline{\Delta})^2|\overline{S}| \tag{6}$$

where C_s is the Smagorinsky constant and set to 0.1, $\overline{\Delta}$ is the filter width

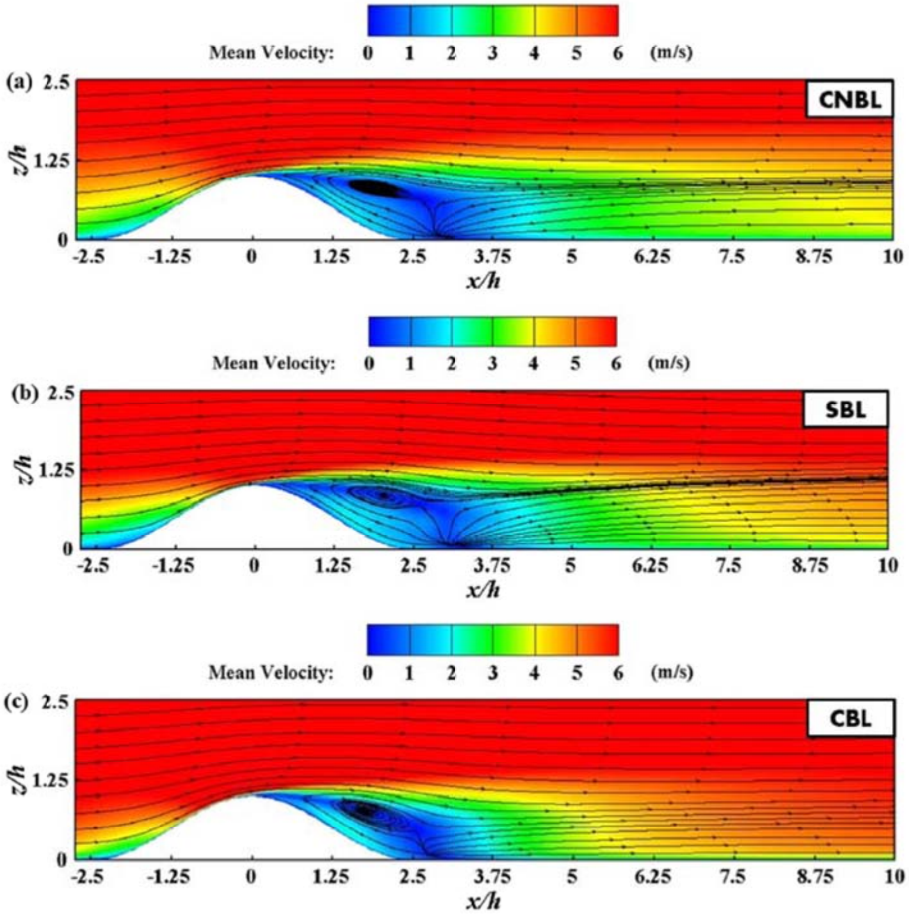

Fig. 7. Contours and streamlines of mean velocity on the vertical plane ($y = 0$) for inversion-capped ABL flows over a steep hill: (a) CNBL, (b) SBL and (c) CBL.

determined by the grid size ($\overline{\Delta} = (\Delta x \Delta y \Delta z)^{1/3}$), and $|\overline{S}|$ is the magnitude of the resolved strain-rate tensor. The subgrid-scale kinetic energy k_{SGS} is estimated by $k_{SGS} = \nu_t |\overline{S}| / C_k$, where C_k is the model constant, taken as 0.0453.

The turbulent Prandtl number is specified by:

$$Pr_t = \left(1 + 2\frac{l}{\overline{\Delta}}\right)^{-1} \tag{7}$$

where l is the stability-dependent length scale given by:

$$l = \begin{cases} min\left(0.76\sqrt{k_{SGS}}\left(\dfrac{g}{\theta_0}\dfrac{\partial\overline{\theta}}{\partial z}\right)^{-1/2}, \overline{\Delta}\right) & \dfrac{|g_i|}{\theta_0}\dfrac{\partial\overline{\theta}}{\partial z} > 0 \\ \overline{\Delta} & \dfrac{|g_i|}{\theta_0}\dfrac{\partial\overline{\theta}}{\partial z} \leq 0 \end{cases} \tag{8}$$

where k_{SGS} is the SGS turbulent kinetic energy.

2.3. Computational domain and grid system

In this study, the same computational configuration is used for the precursor and successor simulations. The domain covers 3 km (x) × 3 km (y) × 1 km (z) for the CNBL and CBL cases, and 2 km (x) × 2 km (y) × 0.8 km (z) for the SBL case. A 3-D hilly terrain model defined by the cosine-based function $z_s(x, y) = h\, cos^2\, \pi (x^2 + y^2)^{1/2} / 2L$ ($h = 80\ m, L = 200\ m$) is placed at the upstream region of the successor computational domain, as depicted in Fig. 1. The maximum slope of the hill is around 32°, which may cause strong flow separation on the leeward side. To minimize artificial perturbations from the inlet boundary in the region of interest, the distance between the inlet plane and the hill model is determined to be more than 10 times the hill height. In addition, the outlet boundary is located at a distance of more than 15 times the hill height downstream of the hill center to allow the hill-induced wake turbulence to fully develop, and the blockage ratio is kept below 2% to avoid introducing unphysical distortions to the flow fields around the hill.

In the precursor simulations, a uniform grid resolution of 8 m is applied to generate both the conventionally neutral and unstably stratified boundary layer flows, and a finer grid spacing of 5 m is adopted to adequately reproduce the characteristics of stably stratified boundary layer flows. For the successor simulations, a local grid refinement strategy is utilized near the hill, aiming to accurately capture the flow structures and turbulent statistics. As illustrated in Fig. 2 (a), a nested grid scheme is used to refine the horizontal grid cells in the target zone, which extends over (L_x, L_y) = (12.5h, 12.5h) in the streamwise and spanwise directions. The normalized horizontal grid spacing in the fine grid domain is set as $\Delta x/h, \Delta y/h = 5 \times 10^{-2}$ based on the grid sensitivity analysis as shown in Zhou et al. (2022). In addition, the terrain-following grid technique shown in Fig. 2 (b) is employed in the vertical direction because it can improve the prediction accuracy of terrain-induced turbulence by reducing the interpolation errors between the curved topographic surface and the computational grid. The minimum vertical grid spacing is specified as $\Delta z_{min}/h = 6.25 \times 10^{-3}$ near the ground surface, which can accurately resolve the turbulent eddy structures around hilly terrain. Furthermore, it is important to note that the spatiotemporal flow variables sampled from the precursor simulation are linearly interpolated at the inlet plane of the successor simulations in both spatial and temporal dimensions. It is also verified that the interpolation error is almost negligible in this study. The total number of grid cells in the successor simulations is about 32.4 million.

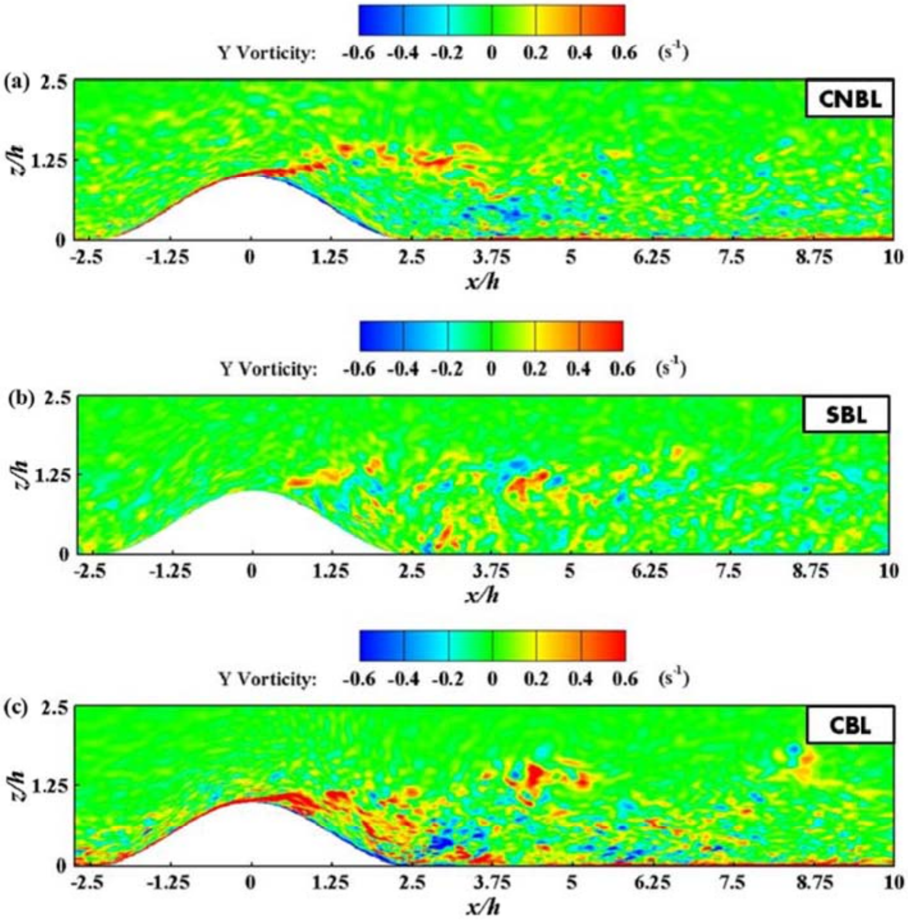

Fig. 8. Contours of spanwise vorticity on the vertical plane ($y = 0$) for inversion-capped ABL flows over a steep hill: (a) CNBL, (b) SBL and (c) CBL.

2.4. Boundary conditions

Proper initialization of the flow field is essential for adequately reproducing the realistic dynamics of ABL flow in the precursor simulation. Based on the analysis of field observation data in the coastal region of Chiba Prefecture, the velocity field is initialized with a uniform geostrophic wind speed of 8 m/s throughout the computational domain in this study. The initial potential temperature profile is prescribed as a constant 300 K below an altitude of 500 m and increases linearly at a rate of 3 K/km up above that height to the upper boundary, as illustrated in Fig. 3.

To incorporate the effects of terrain roughness, the Schumann-Grötzbach model (Schumann, 1975; Grötzbach, 1987) is implemented on the lower surface in both the precursor and successor simulations. The surface-normal shear stress components at the lower boundary are specified as:

$$\tau_{13} = -u_*^2 \frac{\overline{u}(z_1)}{(\langle\overline{u}(z_1)\rangle^2 + \langle\overline{v}(z_1)\rangle^2)^{1/2}} \tag{9}$$

$$\tau_{23} = -u_*^2 \frac{\overline{v}(z_1)}{(\langle\overline{u}(z_1)\rangle^2 + \langle\overline{v}(z_1)\rangle^2)^{1/2}} \tag{10}$$

where z_1 is the height of wall-adjacent cell centers, the angle brackets denote the horizontal averaging operator and u_* is the friction velocity which can be implicitly estimated using the Monin-Obukhov (M-O) similarity law for non-neutral stratification:

$$u_* = -\frac{\kappa(\langle\overline{u}(z_1)\rangle^2 + \langle\overline{v}(z_1)\rangle^2)^{1/2}}{ln\left(\frac{z}{z_0}\right) - \psi_M\left(\frac{z}{L}\right)} \tag{11}$$

$$\psi_M\left(\frac{z}{L}\right) = \begin{cases} (1 - 15(z/L))^{-1/4}, & L < 0 \\ 1 + 4.9(z/L), & L > 0 \end{cases} \tag{12}$$

where z_0 is the roughness length ($z_0 = 0.1\,m$), κ is the von-Kármán constant ($\kappa = 0.4$) and $\psi_M(z/L)$ is the stability correction function for the momentum flux. Furthermore, a similar approach is employed to model the surface temperature flux based on the M-O similarity law.

$$q_* = \frac{u_*\kappa(\theta_s - \langle\overline{\theta}(z_1)\rangle)}{ln\left(\frac{z}{z_0}\right) - \psi_H\left(\frac{z}{L}\right)} \tag{13}$$

$$\psi_H\left(\frac{z}{L}\right) = \begin{cases} (1 - 9(z/L))^{-1/2}, & L < 0 \\ 1 + 7.8(z/L), & L > 0 \end{cases} \tag{14}$$

where θ_s is the surface potential temperature, $\overline{\theta}$ is the filtered potential temperature at the first grid cell and $\psi_H(z/L)$ is the stability correction function for the temperature flux. As demonstrated by Kumar et al. (2010), the characteristics of thermally stratified ABL flows driven by a constant surface temperature flux or a constant surface temperature are in good agreement. In this study, the surface potential temperature is controlled by adjusting the cooling rate C_r from 0.125 K/h to − 0.125 K/h, which corresponds to stable, neutral and unstable stratification conditions. At the upper boundary, the velocity is treated with a slip-wall condition and the potential temperature gradient is prescribed

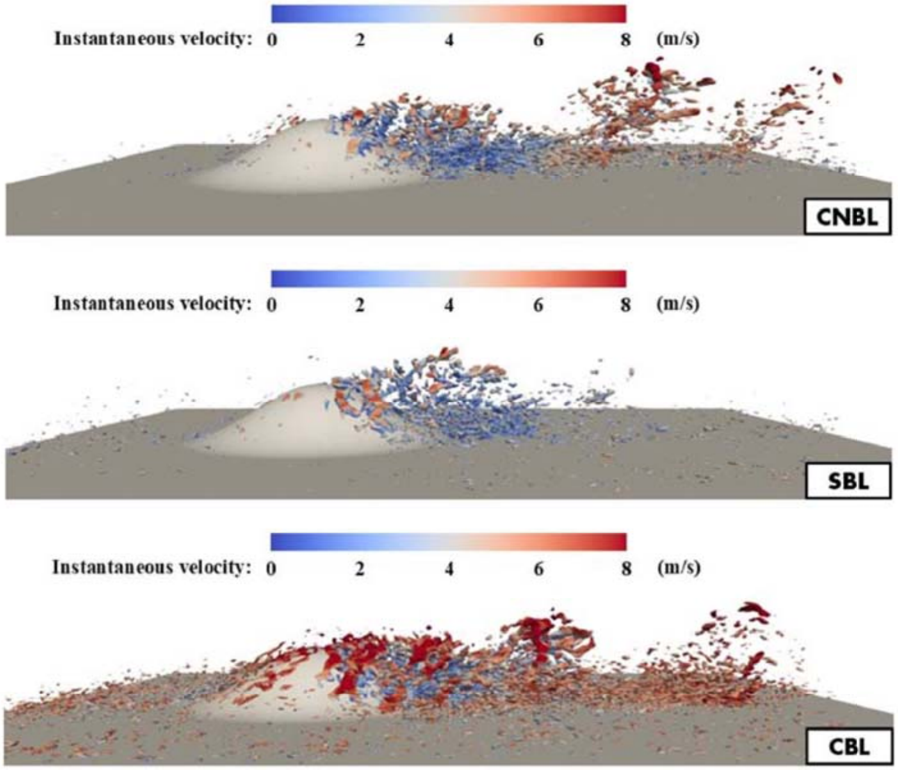

Fig. 9. 3-D view of coherent vortex structures identified by Q-criterion (Q = 0.05) for inversion-capped ABL flows over a steep hill: (a) CNBL, (b) SBL and (c) CBL.

to match the initial temperature profile. Moreover, all lateral boundaries are specified as periodic conditions.

Instead of all periodic lateral boundaries in the precursor simulations, two lateral sides are prescribed as inlet boundaries and the other two are designated as outlet boundaries in the successor simulations. This boundary configuration considers the wind veer effects associated with the Coriolis force, while minimizing the disturbances in the flow field caused by the reflection of wake turbulence structures. The time series of velocity and temperature obtained from the precursor simulations are applied at the inlet planes of the successor simulations. A zero-gradient Neumann condition is applied to both velocity and temperature, while a Dirichlet condition with a fixed value of zero is employed for the modified pressure at the outlet boundaries. Furthermore, the lower and upper boundary conditions in the successor simulations are kept consistent with those in the precursor simulations.

2.5. Numerical schemes and solution strategies

The finite volume method is employed to conduct unsteady LES simulations, and all flow variables are discretized within a collocated unstructured grid system. For the spatial discretization of the governing equations, a second-order linear interpolation scheme is utilized for the convection and diffusion terms, while a second-order implicit backward scheme is applied to the unsteady terms. In addition, the semi-implicit PIMPLE algorithm (a combination of PISO and SIMPLE) is employed for the iterative coupling of pressure and momentum equations for an optimal trade-off between computational accuracy and numerical stability. Moreover, separate algebraic solvers are used for the velocity, temperature and pressure equations. The velocity and temperature equations are solved using the preconditioned bi-conjugate gradient (PBiCG) method with a diagonally incomplete-LU (DILU) preconditioner. For the pressure Poisson equation, a preconditioned conjugate gradient (PCG) method with a generalized geometric-algebraic multigrid (GAMG) pre-conditioner is adopted. The convergence criteria are prescribed as the scaled residuals of all flow variables dropping below 10^{-5} within each time step, and the time step size is set to $\Delta t = 0.1$ s. In this study, all precursor simulations are run for a total of 34,200 s, in which the quasi-equilibrium state of the turbulent flow fields is reached after 28,800 s. The time series of velocity and temperature during the last 5400 s are recorded to build a turbulent inflow database for the successor simulations. Furthermore, in the successor simulations, the first 1800 s are allocated to dissipate the transient effects, and the next 3600 s are used for data sampling and flow analysis in this study. All the simulation cases are conducted on a parallel computing cluster system (Intel Xeon CPU E5-2667 v4 @ 3.20 GHz, 112 cores, 512 GB memory). A summary of the numerical schemes and solution strategies adopted in the LES simulations is listed in Table 1.

3. Model validation

To validate the numerical model for simulating the turbulent flow fields over steep terrain under thermally stratified ABL flows capped with an inversion layer, the validation procedure is divided into two parts: in Section 3.1, the performance of the LES model in reproducing the thermally stratified ABL flows with an inversion-capped layer over flat terrain is investigated, and in Section 3.2, the accuracy of the LES model in predicting turbulent flows over steep terrain is evaluated through a quantitative comparison with wind tunnel tests.

3.1. Thermally stratified ABL flows with an inversion layer over flat terrain

The inversion-capped ABL flows over flat terrain under three typical thermal stability conditions (stable, neutral and unstable) are simulated by the LES model. Consistent with Liu and Stevens (2021), the geostrophic wind speed U_g is set to 8 m/s and the Coriolis parameter f_c is specified as $1.39 \times 10^{-4}\ \mathrm{s}^{-1}$, which corresponds to a latitude of 73° N. The potential temperature field is initialized using a piecewise-linear function as $\theta = 265\ \mathrm{K}\ (z \leq 100\ \mathrm{m})$ and $\theta = 265\ \mathrm{K} + 0.01 \times (z - 100)\ (z > 100\ \mathrm{m})$, and the surface cooling rate C_r is prescribed as 0.25

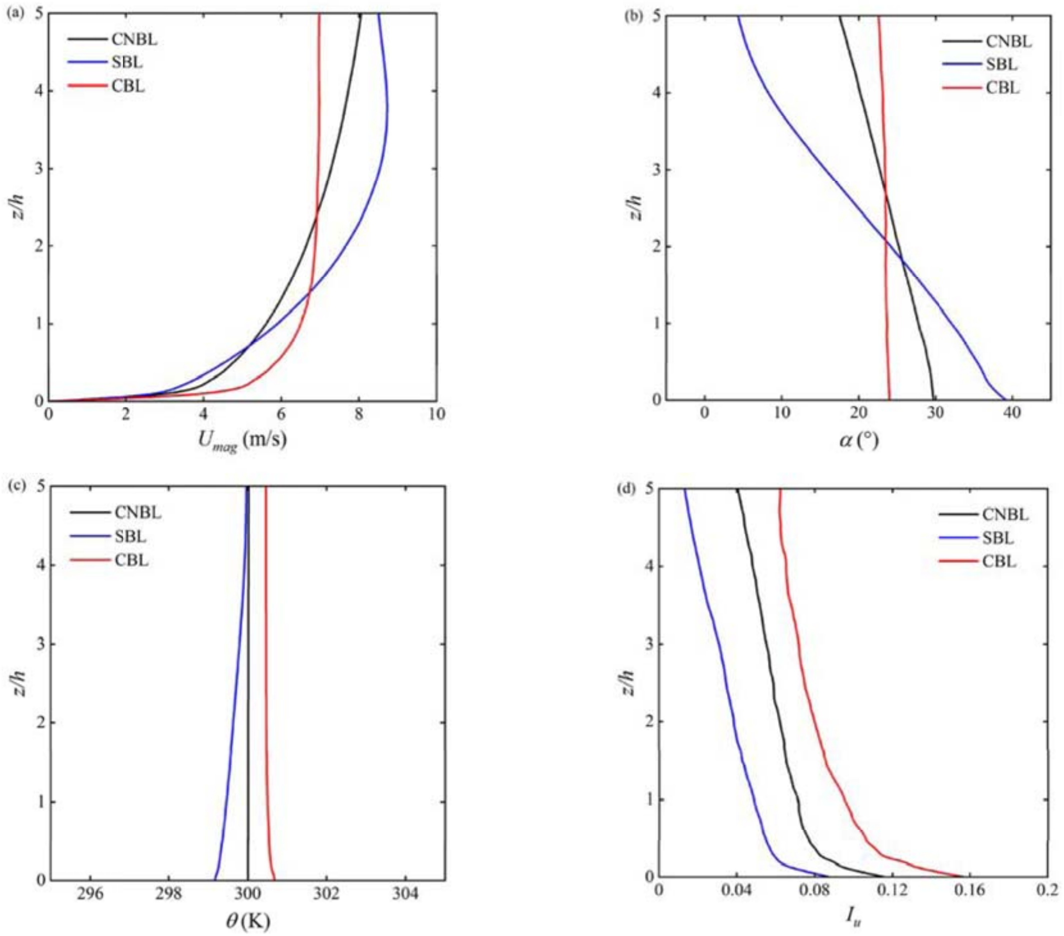

Fig. 10. Characteristics of oncoming inversion-capped ABL flows: (a) mean wind speed, (b) mean wind direction, (c) mean potential temperature and (d) turbulence intensity.

K/h for the stable case and −0.25 K/h for the unstable case. Moreover, the ground roughness lengths for both momentum and heat are assigned to 0.1 m. Furthermore, all LES simulations are performed for a total of 32,400 s, and the statistical analysis is conducted using simulation data sampled during the final 3,600 s.

The vertical profiles of the mean wind speed, wind direction, potential temperature and total turbulent momentum flux are plotted in Fig. 4. The LES results by Liu and Stevens (2021) are selected as a reference for validation purposes. The statistical characteristics of SBL, CNBL and CBL reproduced by the present LES model show good agreement with those of a previous study validated by Gadde and Stevens, 2021 for inversion-capped ABL flows under different thermal stratifications. As illustrated in Fig. 4(a), the wind speed in the SBL rapidly reaches a maximum at low altitudes and then gradually approaches the geostrophic wind speed, forming a low-level jet. Similar to the SBL, the wind speed in the CNBL exceeds the geostrophic wind speed at a certain height due to the presence of an upper inversion layer, an atmospheric phenomenon known as super-geostrophic jet. In contrast, the wind speed does not exhibit a steep gradient in the CBL due to vigorous convective mixing. In addition, the wind veer effect is strongest in the SBL and weakest in the CBL, as demonstrated in Fig. 4(b). Since vertical mixing is enhanced by the positive buoyancy force associated with surface heating, the wind speed profile in the CBL becomes more uniform, thereby reducing the overall veer effect. Moreover, Fig. 4(c) reveals that the vertical distribution of mean potential temperature varies significantly across different thermal stability regimes. In the SBL, the potential temperature increases with height due to the inversion layer. However, in the CBL, it slightly decreases with height due to buoyant mixing induced by surface heating. Furthermore, Fig. 4(d) shows that the turbulent momentum flux is lowest in the SBL and highest in the CBL. This is because that stable stratification suppresses turbulence fluctuations, while unstable stratification enhances turbulent motions.

3.2. Turbulent flow fields over steep terrain

The performance of the present LES model in predicting turbulent flow fields over steep terrain is validated against laboratory experiments (Ishihara et al., 2001). The geometry of hill model in the wind tunnel test is identical to that used in the subsequent simulations. In addition, the grid refinement strategies and numerical schemes adopted in this section are the same as those in the subsequent simulations. To maintain the numerical accuracy and stability of time-dependent calculations, the CFL (Courant-Friedrichs-Lewy) number is limited to less than 1 throughout the entire computational domain. Moreover, data sampling is conducted from 3 to 9 s since it is observed that the initial transient effects diminish after the first 3 s.

The vertical distributions of the mean velocity and turbulence intensity around the hilly terrain are displayed in Fig. 5. For comparison, the mean velocity and the root mean square of velocity fluctuation are normalized by the freestream velocity U_{ref}. Overall, the profiles of turbulent statistics predicted by LES simulations are in good agreement with the experimental data. It is demonstrated that the present LES model can well capture the flow dynamics over hilly terrain. First, as illustrated in Fig. 5(a), both the pronounced wind speed-up effects at the hilltop and the strong flow separation on the leeward slope are

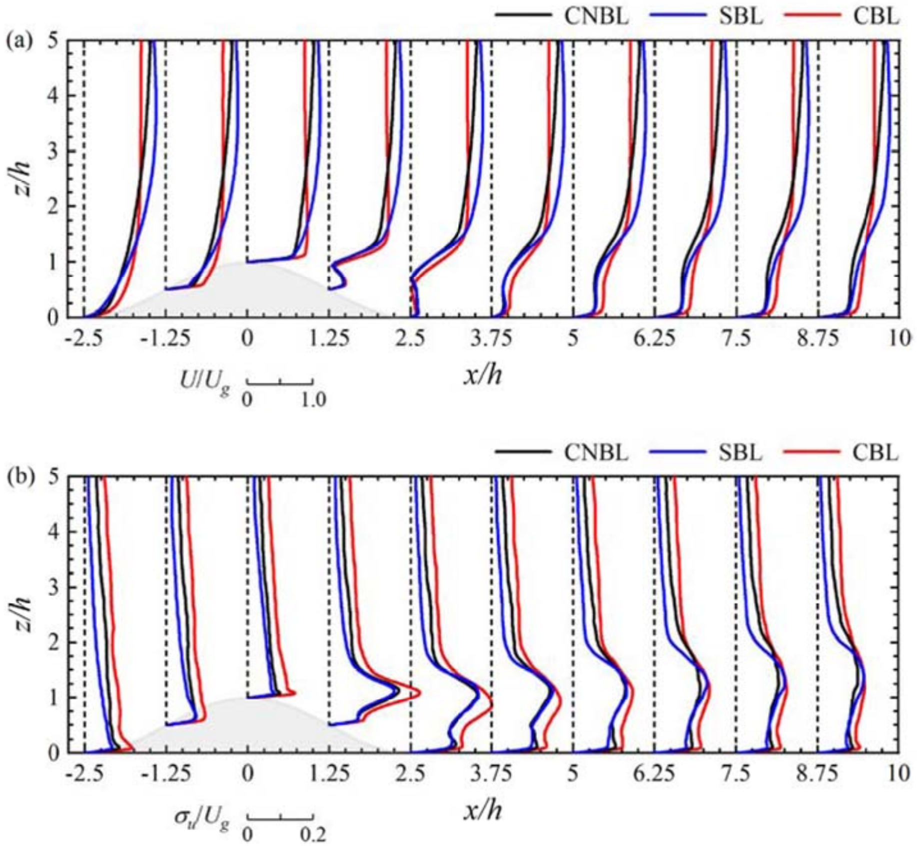

Fig. 11. Vertical distribution of turbulence properties for inversion-capped ABL flows over a steep hill on the $y/h = 0$ plane: (a) mean velocities and (b) turbulence fluctuations.

accurately captured. Second, as the wind flow propagates downstream, the large velocity deficit in the near-wake region is gradually recovered in the far-wake region due to turbulent mixing, flow reattachment and wake expansion. Third, in contrast to the upwind side, the turbulence intensity is amplified on the downwind side due to the formation of a highly unstable and separated turbulent shear layer, as shown in Fig. 5 (b).

4. Results and discussions

The flow structures and turbulence characteristics of the inversion-capped ABL flows over steep terrain under neutral, stable and unstable stratification conditions are investigated in Sections 4.1 and 4.2. The proposed wind speed prediction model for the inversion-capped ABL flows over a steep hill is described in Section 4.3.

4.1. Flow structures

The mean velocity contours and streamlines along the horizontal plane of $z/h = 3/4$ for various inversion-capped thermally stratified ABL flows over a steep hill are presented in Fig. 6. In general, a pair of recirculating vortices is formed on the leeward side due to the strong flow separation induced by sudden increase in the adverse pressure gradient downstream of the hill crest. Moreover, the hill wake is deflected to the left ($y/h > 0$) due to the lateral wind shear caused by the Coriolis force. The stronger the stratification, the greater the deflection of the wake trajectory. Thus, a strongly asymmetric wake pattern is observed in the SBL, while it remains nearly symmetric in the CBL.

The vertical distribution of mean velocity streamlines across the hill's center plane of $y = 0$ under different thermally stratified ABL flows is illustrated in Fig. 7. Overall, the streamlines rise as the flow approaches the hill crest, which is caused by the flow convergence and acceleration on the upstream side. After the flow passes the hill crest, a large separation bubble develops on the lee side. Within the separation bubble, the flow near the surface reverses direction due to the low-pressure region caused by flow separation. Furthermore, in the SBL, the streamlines associated with the separation bubble remain elevated in the far wake region due to the suppression of downward mixing by the stable stratification. In contrast, the streamlines leading to the separation bubble are nearly horizontal in the CBL because of the enhanced vertical mixing induced by the unstable stratification.

In addition to the time-averaged flow behaviors, it is also interesting to examine instantaneous flow structures of the inversion-capped ABL flows over a steep hill. Fig. 8 plots the contours of spanwise vorticity in the vertical plane of $y = 0$. In both the CNBL and CBL, a thin layer of strong positive vorticity (shown in red) is distributed on the upwind side of the hill. However, this phenomenon is not observed in the SBL. Due to the absence of buoyant convection and convective updrafts, the vorticity generation near the upslope is suppressed in the SBL. Moreover, the magnitude of spanwise vorticity is enhanced on the leeward side of the hill owing to flow separation and vortex shedding. Furthermore, the intensity of turbulent wake vortices increases as atmospheric stability decreases, which can be attributed to enhanced vertical mixing and shear layer instability under unstable stratification.

Fig. 9 shows a 3-D view of coherent vortex structures identified by the Q-criterion for various inversion-capped ABL flows over a steep hill. In the SBL, the formation and shedding of vortex in the wake region are significantly attenuated due to the damping effect of negative buoyancy forces. Conversely, in the CBL, the presence of positive buoyancy forces enhances turbulence and mixing, resulting in stronger vortex structures.

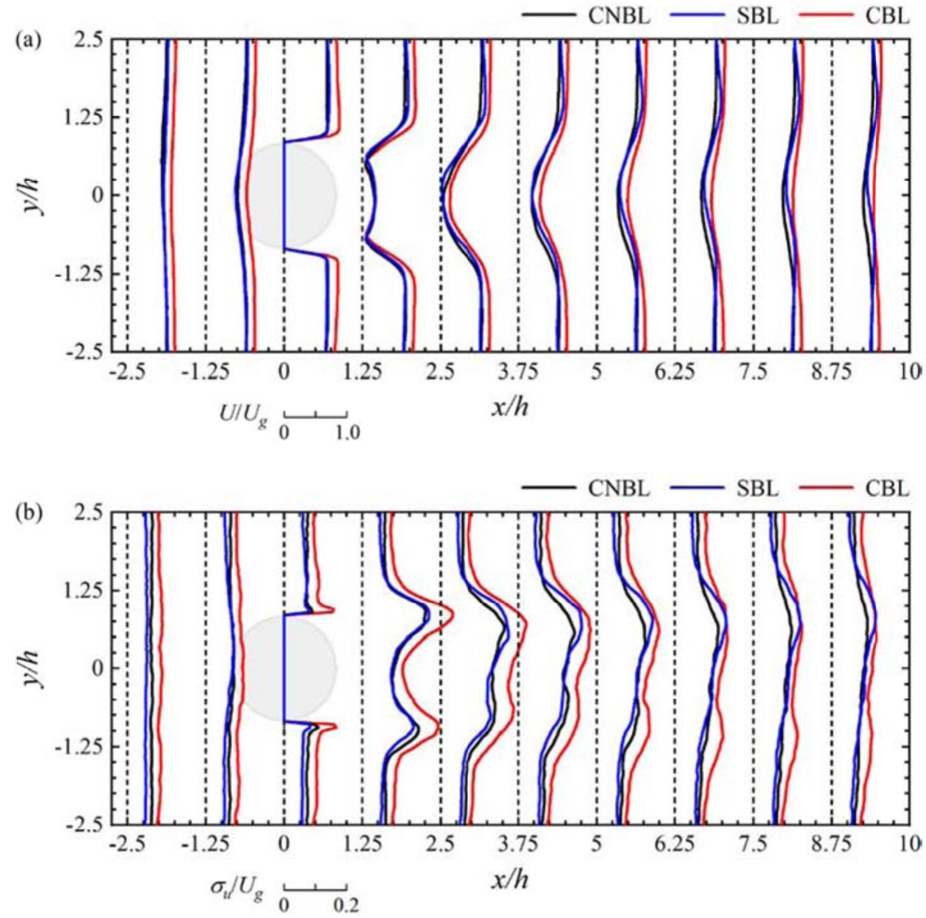

Fig. 12. Horizontal distribution of turbulence properties for inversion-capped ABL flows over a steep hill on the $z/h = 3/4$ plane: (a) mean velocities and (b) turbulence fluctuations.

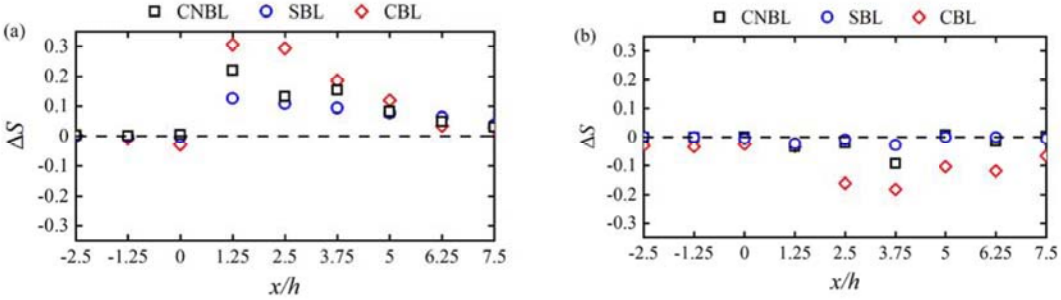

Fig. 13. Longitudinal distribution of ΔS for inversion-capped ABL flows over a steep hill in the plane of $y/h = 0$ plane at (a) $z'/h = 1/2$ and (b) $z'/\ h =\ 1$.

4.2. Turbulence characteristics

The mean flow and turbulence fluctuations of inversion-capped ABL flow under stable, neutral and unstable stratification conditions are illustrated in Fig. 10. The wind shear, wind veer as well as potential temperature gradient are most pronounced in the SBL, but weakest in the CBL. In addition, the mean potential temperature near the surface remains nearly constant at 300 K in the CNBL because the surface potential temperature flux is almost negligible. Due to surface cooling, the potential temperature decreases in the lower part of the SBL and gradually increases with height. Conversely, the potential temperature increases in the lower part of the CBL compared to the CNBL, and the potential temperature is almost uniform in this region due to the efficient vertical mixing driven by buoyancy-generated turbulence. Furthermore, consistent with field observations, the turbulence intensity is amplified in the CBL and diminished in the SBL.

The vertical profiles of normalized mean velocities and turbulence fluctuations at the plane of $y/h = 0$ for different inversion-capped ABL flows over a steep hill are shown in Fig. 11. For comparison purposes, the same geostrophic wind speed used to drive the inversion-capped ABL flows is employed for normalization. The mean wind speed and turbulence intensity upstream of a steep hill are mainly driven by the characteristics of the oncoming ABL flows. The strongest wind shear and the weakest turbulence fluctuation are observed in the SBL. In addition, the wind speed-up at the hilltop is more pronounced in the SBL. This is because the stronger velocity gradient near the surface amplifies the local acceleration over the hill crest. When the wind flows over the hilltop, a large velocity deficit is identified in the near-wake region,

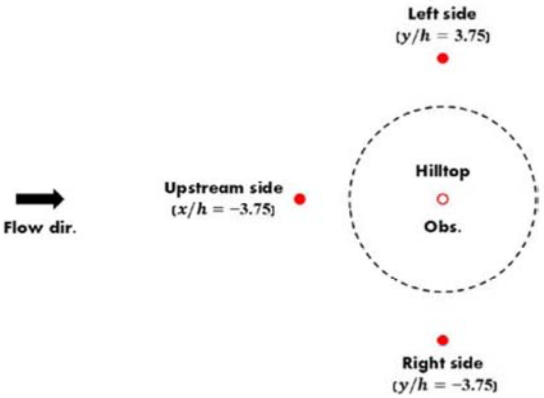

Fig. 14. Four locations of inversion-capped ABL flows around a steep hill.

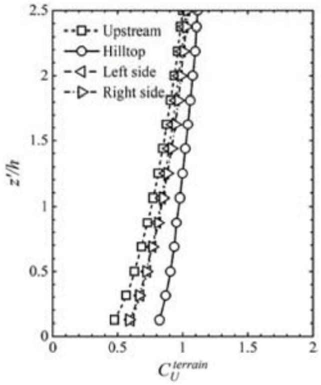

Fig. 15. Vertical distribution of terrain correction factors for CNBL flows over a steep hill.

which is characterized by intense flow separation. It is noteworthy that the wake recovery is faster in the SBL due to the stronger channeling effects between the boundary layer and the topography. Furthermore, it is demonstrated that wake turbulence fluctuations are more pronounced in the CBL due to enhanced vertical mixing induced by positive buoyancy forces.

Fig. 12 shows the horizontal profiles of mean velocities and turbulence fluctuations at the plane of $z/h = 3/4$ for different inversion-capped ABL flows over steep hill. Overall, the mean wind speed and turbulence intensity exhibit nearly symmetrical distributions on the windward side of the steep hill under different inversion-capped ABL flow conditions. However, the spanwise patterns of turbulence statistics in the wake region are found to be sensitive to atmospheric stratification. As atmospheric stratification increases, the wake patterns become increasingly asymmetric due to stronger wind veer effects in the SBL. This asymmetry is induced by a significant wake deflection in the SBL, which shifts the locations of the maximum velocity deficit and turbulence intensity towards the left side ($y/h > 0$).

A quadrant analysis based on the Reynolds stress is conducted to quantitatively identify turbulent coherent structures over a steep hill under different inversion-capped ABL flow conditions. The four quadrants of Reynolds stress are expressed as follows:

$$S_n(uw) = \begin{cases} -\overline{uw} & \text{for } (u > 0, w > 0) \quad \text{if } n = 1 \\ -\overline{uw} & \text{for } (u < 0, w > 0) \quad \text{if } n = 2 \\ -\overline{uw} & \text{for } (u < 0, w < 0) \quad \text{if } n = 3 \\ -\overline{uw} & \text{for } (u > 0, w < 0) \quad \text{if } n = 4 \end{cases} \tag{15}$$

where u and w are the streamwise and vertical fluctuating velocity components, respectively. Quadrants $S_1(uw)$ and $S_3(uw)$ show negative contributions to the Reynolds stress, implying the outward and the inward motions, respectively, while quadrants $S_2(uw)$ and $S_4(uw)$ make positive contributions to the Reynolds stress, indicating the ejection and the sweep motions, respectively. The difference ΔS ($= S_4(uw) - S_2(uw)$) reveals the strength of organized turbulent motions.

Fig. 13 presents the longitudinal distribution of ΔS over steep terrain at two representative elevations of $z'/h = 1/2$ and 1, where $z' = z - z_s$ and z_s stands for the elevation of terrain surface. It is found ΔS are almost zero on the windward side of the hill and are independent of the atmospheric stability conditions. This indicates that the organized motions in the upstream region are relatively weak, regardless of the thermal stratification. In contrast, ΔS on the leeward side of the hill deviates significantly from zero, indicating the presence of strong organized motions. As atmospheric stability increases, the intensity of the organized motions decreases. Furthermore, it is confirmed that the sweep motions ($u > 0, w < 0$) are dominant at the lower elevation of $z'/h = 1/2$, while the ejection motions ($u < 0, w < 0$) are observed at the higher elevation of $z'/h = 1$. The strength of organized motions in the wake of the hill gradually decreases shown in Fig. 9.

4.3. Wind speed prediction model for inversion-capped ABL flows over topography

As mentioned in Yamaguchi et al. (2024) and Zhou and Ishihara (2025), the vertical profiles of the mean wind speed over complex terrain under stable and unstable stratification can be reasonably predicted by Eq. (16). The effects of topography and thermal stratification can be separated, and can be expressed as follows:

$$U_{tar}^{pred}(x, y, z') = U_{obs}^{neutral} \times C_U^{terrain}(x, y, z') \times C_U^{stability}(z') \tag{16}$$

where $U_{obs}^{neutral}$ denotes the mean wind speed at the observation point under neutral stratification, $C_U^{terrain}(x, y, z')$ is the terrain correction factor calculated from the CFD model of wind flows over complex terrain under neutral stratification and $C_U^{stability}(z')$ is the stability correction factor derived based on the Monin-Obukhov similarity theory (Monin and Obukhov, 1954).

However, it should be noted that these studies did not consider the effects of free-atmospheric stratification. In reality, the ABLs are rarely truly neutral since thermal stratification is typically present in the free atmosphere. Due to the presence of an upper-level potential temperature inversion, the vertical structures of an inversion-capped ABL may differ significantly from an ABL without the influence of an inversion. It is therefore questionable whether the previous approaches that neglected free-atmosphere stratification can be applied to predict the profiles of mean wind speed over topography under inversion-capped ABL flow conditions.

To account for the influence of topography on the mean flow fields over a steep hill, terrain correction factors at several representative locations—such as the upstream region, hilltop, and lateral sides (Fig. 14) are derived from LES simulations of wind flow over a steep hill under an inversion-capped neutrally stratified ABL (CNBL) condition, as shown in Fig. 15. The terrain correction factor is defined as:

$$C_U^{terrain}(x, y, z') = \frac{U_{terrain}^{CNBL}(x, y, z')}{U_{obs}^{CNBL}} \tag{17}$$

where U_{obs}^{CNBL} denotes the mean wind speed at the observation point of $z'/h = 1.25$ above the hilltop and $U_{terrain}^{CNBL}(x, y, z')$ stands for the mean wind speed profiles over the hill.

Regarding the effect of atmospheric stratification, a stability correction factor is derived by considering the effect of the free-atmosphere lapse rate:

$$C_U^{stability}(z') = \frac{U_{SBL\ or\ CBL}(z') / U_{SBL\ or\ CBL}(z_{ref})}{U_{CNBL}(z') / U_{CNBL}(z_{ref})} \tag{18}$$

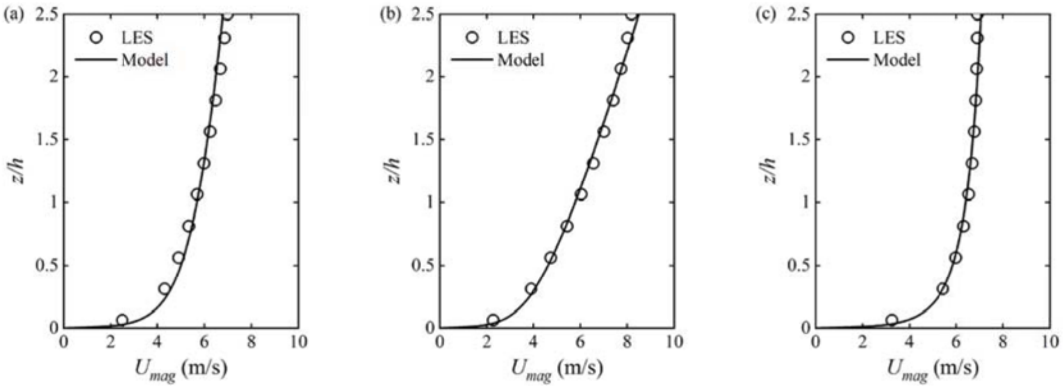

Fig. 16. Comparison of mean wind speed profiles predicted by LES and analytical model for incoming inversion-capped ABL flows: (a) CNBL, (b) SBL and (c) CBL.

Table 2
Characteristics of incoming inversion-capped thermally stratified ABL flows used in this study.

Case	U_g (m/s)	f_c (s^{-1})	z_0 (m)	γ_θ (K/km)	C_r (K/h)	u_* (m/s)	L (m)
CNBL	8	8.55 × 10^{-5}	0.1	3	0	0.326	–
SBL					0.125	0.262	224
CBL					−0.125	0.403	−682

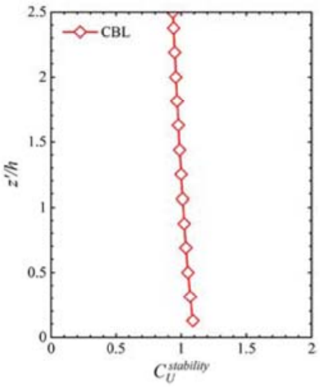

Fig. 17. Vertical distribution of stability correction factors for the CBL.

where U_{SBL}, U_{CBL} and U_{CNBL} refer to the mean wind speed profiles of the inversion-capped ABL flows under stable, unstable and neutral stratification conditions, respectively, z_{ref} denotes the reference height of $z' = 1.25h$ above flat terrain. Here h is 80 m.

For CNBL flows, the profile of mean wind speed within the surface layer can be well described by a modified logarithmic law (Abkar and Porté-Agel, 2013) as shown in Eq. (15), which adds an additional correction term to reflect the influence of free-atmosphere stratification.

$$U_{CNBL} = \frac{u_*}{\kappa} ln\frac{z}{z_0} + 0.3N_\infty(z - z_0), N_\infty = \sqrt{(g/\theta_0)\gamma_\theta} \tag{19}$$

where u_* is the friction velocity, z_0 is the surface roughness length, N_∞ denotes the Brunt-Väisälä frequency related to the free-atmosphere lapse rate γ_θ.

In both SBL and CBL flows, the Monin-Obukhov similarity theory is universally adopted to modify the pure logarithmic law by introducing a stability correction term that accounts for the effects of surface thermal stratification. Therefore, the mean wind speed profile in the surface layer in the CBL flow can be expressed as follows:

$$U_{CBL} = \frac{u_*}{\kappa}\left(ln\frac{z}{z_0} - \psi_{CBL}\left(\frac{z}{L}\right)\right) \tag{20}$$

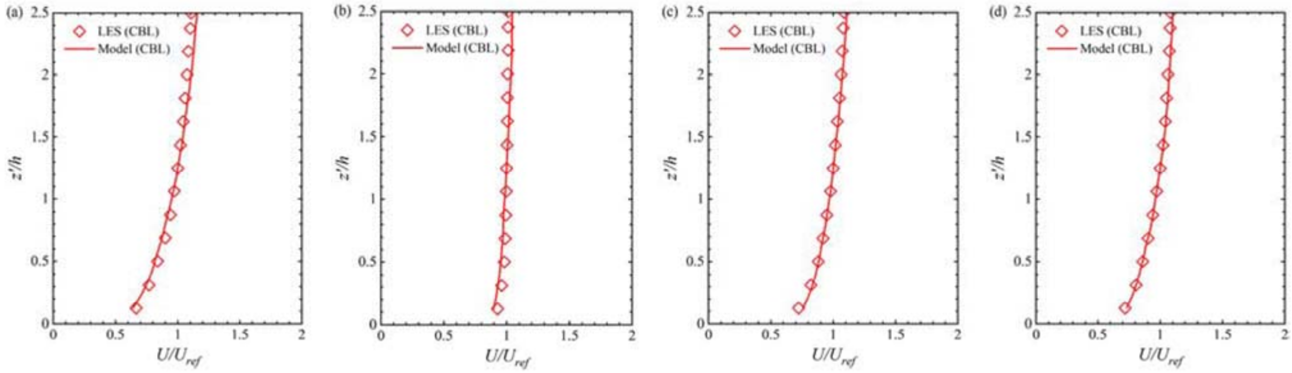

Fig. 18. Comparison of mean wind speed profiles over a steep hill in the CBL predicted by the proposed model and LES simulations: (a) upstream side, (b) hilltop, (c) left side and (d) right side.

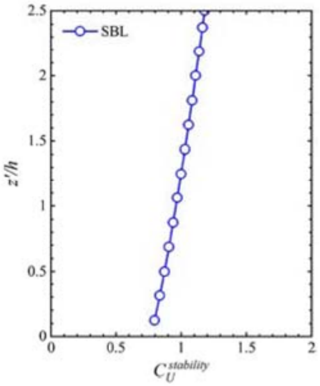

Fig. 19. Vertical distribution of stability correction factors for the SBL flow.

$$\psi_{CBL}\left(\frac{z}{L}\right) = 2\,ln\left(\frac{1+x}{2}\right) + ln\left(\frac{1+x^2}{2}\right) - 2\,tan^{-1}x + \frac{\pi}{2}, x = \left(1-16\frac{z}{L}\right)^{1/4} \tag{21}$$

Moreover, Narasimhan et al. (2024) derived a new analytical model that coupled the Ekman layer and surface layer in the SBL flow, in which the mean wind speed profile in the surface layer can be formulated as follows:

$$U_{SBL} = \frac{u_*}{\kappa}\left(ln\frac{z}{z_0} - \psi_{SBL}\left(\frac{z}{L}\right)\right) + 0.3N_\infty(z-z_0) \tag{22}$$

$$\psi_{SBL}\left(\frac{z}{L}\right) = -5\frac{z-z_0}{L} \tag{23}$$

Fig. 16 shows a comparison between the analytical wind speed model and the corresponding LES data for the incoming inversion-capped ABL flows under various thermal stratifications. Overall, a reasonable agreement is observed, implying the reliability of the analytical wind speed model. The characteristics of the incoming inversion-capped ABL flows are summarized in Table 2.

The accuracy of the wind speed prediction model over steep terrain is first examined in the context of inversion-capped CBL flows. Based on the stability correction factor defined in Eq. (18), the vertical distribution of correction ratio for the CBL is plotted in Fig. 17. It is shown that the stability correction ratio for the CBL decreases with height due to enhanced vertical mixing, as buoyancy-driven turbulence transports high-momentum air downward from aloft.

Fig. 18 illustrates the predicted and simulated vertical profiles of the mean wind speed of the inversion-capped CBL flow over a steep hill. The predicted profiles are in good agreement with those from the LES simulations, indicating that the proposed model is applicable in capturing the mean wind speed of CBL flow over complex terrain. To the best of the authors' knowledge, this is the first systematic evaluation of the model accuracy using high-fidelity LES results over steep hilly terrain, regarding the performance of analytical wind speed models in predicting mean wind speed profiles over complex terrain under inversion-capped ABL conditions.

The reliability of the proposed model is further assessed for an inversion-capped SBL flow over a steep hill. As shown in Fig. 19, the stability correction factor increases with height because the turbulence suppression under stable stratification reduces the momentum dissipation toward the surface.

Fig. 20 presents the predicted and simulated vertical distributions of mean wind speed for the inversion-capped SBL flow over steep hilly terrain. Overall, the proposed model can reasonably predict the mean wind speed profiles over a steep hill in the inversion-capped SBL. However, the mean wind speed above the hill crest is overestimated in the upper region by the proposed model because the uplift of the low-level jet is constrained by buoyancy forces associated with stable stratification.

To address the overestimation of mean wind speeds at the hilltop by the proposed model in the inversion-capped SBL flow, the σ-coordinate transformation technique is applied to reflect the suppression of vertical fluid motions. The σ-coordinate system is defined as:

$$\sigma(x,y) = \frac{z - z_s(x,y)}{z_{top} - z_s(x,y)} \tag{24}$$

where $z_s(x,y)$ is the terrain height and $z_{top} = 2.5h$ is the height of the upper boundary. Fig. 21 plots the distribution of σ around the hill.

Accordingly, the modified terrain correction factor and the stability correction factor in the σ-coordinate system are expressed as follows:

$$C_U^{terrain}(x,y,\sigma) = \frac{U_{terrain}^{CNBL}(x,y,\sigma)}{U_{obs,\sigma}^{CNBL}} \tag{25}$$

$$C_U^{stability}(\sigma) = \frac{U_{SBL}(\sigma)/U_{SBL}(\sigma_{ref})}{U_{CNBL}(\sigma)/U_{CNBL}(\sigma_{ref})} \tag{26}$$

where $U_{obs,\sigma}^{CNBL}$ is the mean wind speed at the observation point $\sigma = 0.5$ ($z' = 0.75h$) above the hill crest and σ_{ref} is the reference height $\sigma = 0.5$ ($z' = 1.25h$) above the flat terrain. The vertical distributions of the terrain correction factor and the stability correction factor in the σ coordinate system are shown in Fig. 22.

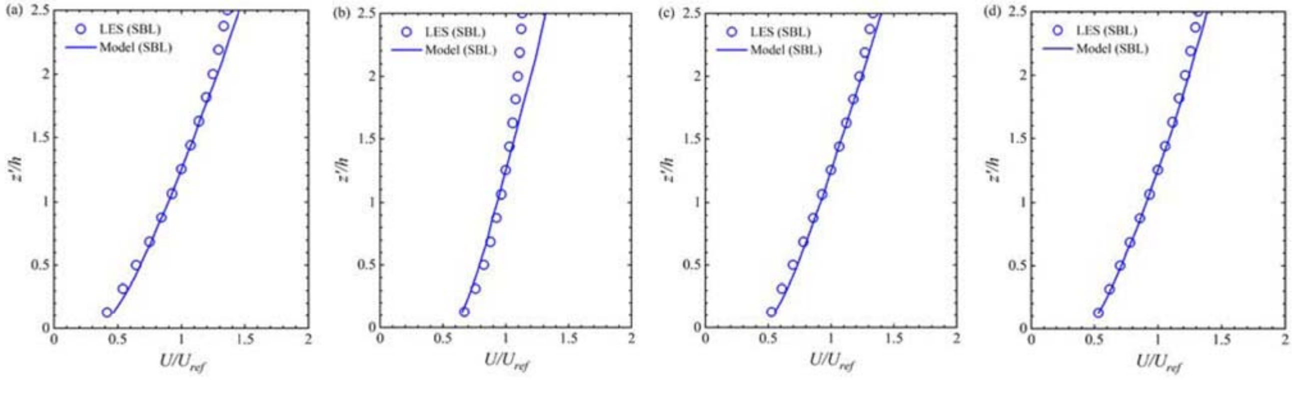

Fig. 20. Comparison of mean wind speed profiles over a steep hill in the SBL predicted by the proposed model and LES simulations: (a) upstream side, (b) hilltop, (c) left side and (d) right side.

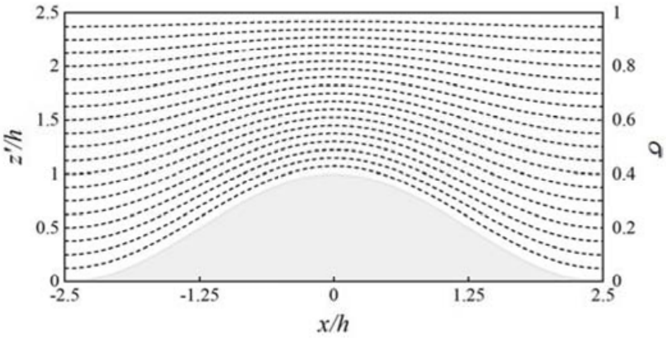

Fig. 21. Schematic of σ-coordinate system around steep topography.

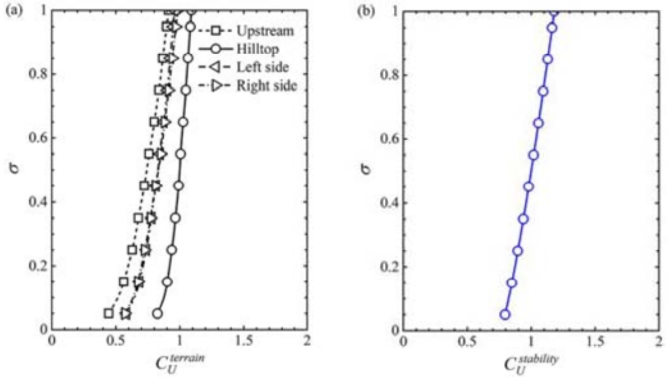

Fig. 22. Vertical distribution of (a) terrain correction factors and (b) stability correction factors in the σ-coordinate system.

Following the transformation from the Cartesian coordinate system to the σ-coordinate system, the above approach for predicting mean wind speed profiles in inversion-capped SBL flows over topography can be reformulated as:

$$U_{tar}^{SBL}(x,y,\sigma) = U_{obs,\sigma}^{CNBL} \times C_U^{terrain}(x,y,\sigma) \times C_U^{stability}(\sigma) \tag{27}$$

Fig. 23 shows the vertical profiles of the mean wind speed over steep hilly terrain predicted by the analytical model using the σ coordinate system. An improved prediction at the hill crest is observed compared to that obtained using the Cartesian coordinate system, as shown in Fig. 23 (b).

5. Conclusions

In this study, the characteristics of various inversion-capped ABL flows over steep terrain are investigated by employing full-scale LES simulations. The numerical model for simulating inversion-capped ABL flows over flat terrain and turbulent flow fields over steep terrain is validated. The flow patterns and turbulent statistics over a steep hill under different inversion-capped ABL flows are clarified. Finally, a wind speed prediction model for inversion-capped ABL flows over steep terrain is proposed. The main conclusions of this study are briefly summarized as follows:

1. The wake structures downstream of the hill crest are significantly affected by atmospheric stratification. In the inversion-capped SBL, an asymmetric flow pattern with a pronounced wake deflection is observed on the leeward side of the hill. As atmospheric stratification increases, the organized motions in the wake region are significantly suppressed.
2. Larger speedup at the hilltop and faster recovery in the hill wake are observed in the inversion-capped SBL due to the presence of a low-level jet and the pronounced channeling effect between the hill and the lower boundary layer. Moreover, the velocity fluctuations are more intense in the inversion-capped CBL over a steep hill due to enhanced vertical turbulence mixing.
3. The mean wind speed profiles of the inversion-capped CBL flow over steep terrain can be accurately predicted by the proposed model, which accounts for the effects of terrain, surface-layer thermal stability and free-atmosphere stratification. Furthermore, the reliability of the proposed model in predicting the inversion-capped SBL flow over a steep hill can be improved by transforming the coordinate system from Cartesian to σcoordinates, in order to consider the effect of buoyancy forces caused by stable stratification on the uplift of the low-level jet.

The results of this study have both theoretical significance and practical value. First, it provides new insight into the impact of atmospheric stratification on wind flow characteristics over hilly terrain. Second, a novel analytical model is developed to predict mean wind speed profiles over complex terrain considering the effects of atmospheric stratification. This model will be beneficial for engineering applications such as wind resource assessment and micro-sitting of wind farms in mountainous regions. Further validation with field measurements under real terrain conditions is essential to demonstrate the applicability and versatility of the proposed model.

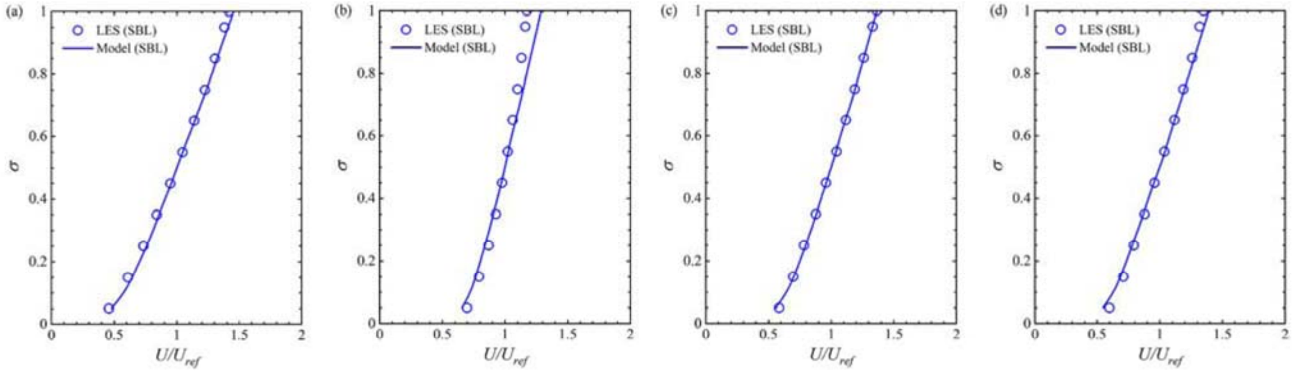

Fig. 23. Comparison of mean wind speed profiles over steep topography in the SBL predicted by the proposed approach and LES simulations in the σ-coordinate system: (a) upstream side, (b) hilltop, (c) left side and (d) right side.

CRediT authorship contribution statement

Tong Zhou: Writing – original draft, Visualization, Software, Investigation, Formal analysis, Data curation. **Takeshi Ishihara:** Writing – review & editing, Validation, Supervision, Resources, Methodology, Conceptualization.

Declaration of competing interest

The authors declare that they have no known competing financial interests or personal relationships that could have appeared to influence the work reported in this paper.

Acknowledgment

This research is conducted as a part of the joint program for next generation energy infrastructure with Toshiba Energy Systems & Solutions Corporation, J-POWER, Shimizu Corporation, Class NK, Tokyo Gas, CHOBU Electric Power. The invaluable assistance provided by the concerned parties during the present investigation is greatly acknowledged. The authors also want to express their sincere gratitude to the China Scholarship Council (Grant No. CSC202107090014) for the funding support.

Data availability

Data will be made available on request.

References

Abkar, M., Porté-Agel, F., 2013. The effect of free-atmosphere stratification on boundary-layer flow and power output from very large wind farms. Energies 6 (5), 2338–2361. https://doi.org/10.3390/en6052338.

Cao, S., Tamura, T., 2006. Experimental study on roughness effects on turbulent boundary layer flow over a two-dimensional steep hill. J. Wind Eng. Ind. Aerod. 94 (1), 1–19. https://doi.org/10.1016/j.jweia.2005.10.001.

Cao, S., Tamura, T., 2007. Effects of roughness blocks on atmospheric boundary layer flow over a two-dimensional low hill with/without sudden roughness change. J. Wind Eng. Ind. Aerod. 95 (8), 679–695. https://doi.org/10.1016/j.jweia.2007.01.002.

Cao, S., Wang, T., Ge, Y., Tamura, Y., 2012. Numerical study on turbulent boundary layers over two-dimensional hills—effects of surface roughness and slope. J. Wind Eng. Ind. Aerod. 104, 342–349. https://doi.org/10.1016/j.jweia.2012.02.022.

Carpenter, P., Locke, N., 1999. Investigation of wind speeds over multiple two-dimensional hills. J. Wind Eng. Ind. Aerod. 83 (1–3), 109–120. https://doi.org/10.1016/S0167-6105(99)00065-3.

Chang, C.Y., Schmidt, J., Dörenkämper, M., Stoevesandt, B., 2018. A consistent steady state CFD simulation method for stratified atmospheric boundary layer flows. J. Wind Eng. Ind. Aerod. 172, 55–67. https://doi.org/10.1016/j.jweia.2017.10.003.

Chen, X., Ishihara, T., 2025. Numerical study of turbulent flows over complex terrain using an unsteady Reynolds-Averaged Navier-Stokes model with a new method for turbulent inflow generation. J. Wind Eng. Ind. Aerod. 257, 105991. https://doi.org/10.1016/j.jweia.2024.105991.

Churchfield, M.J., Lee, S., Michalakes, J., Moriarty, P.J., 2012. A numerical study of the effects of atmospheric and wake turbulence on wind turbine dynamics. J. Turbul. 13 (14), 1–32. https://doi.org/10.1080/14685248.2012.668191.

Ferreira, A.D., Lopes, A.M.G., Viegas, D.X., Sousa, A.C.M., 1995. Experimental and numerical simulation of flow around two-dimensional hills. J. Wind Eng. Ind. Aerod. 54, 173–181. https://doi.org/10.1016/0167-6105(94)00040-K.

Gadde, S.N., Stevens, R.J., 2021. Interaction between low-level jets and wind farms in a stable atmospheric boundary layer. Phys. Rev. Fluids 6 (1), 014603. https://doi.org/10.1103/PhysRevFluids.6.014603.

Grötzbach, G., 1987. Direct numerical and large eddy simulation of turbulent channel flows. Encycl. Fluid Mech. 6, 1337–1391.

Ishihara, T., Fujino, Y., Hibi, K., 2001. A wind tunnel study of separated flow over a two-dimensional ridge and a circular hill. J. Wind Eng. 89, 573–576.

Ishihara, T., Hibi, K., 1998. An experimental study of turbulent boundary layer over steep hills. In: Proceedings of the 15th Japan National Symposium on Wind Engineering, pp. 61–66.

Ishihara, T., Hibi, K., 2002. Numerical study of turbulent wake flow behind a three-dimensional steep hill. Wind Struct. 5, 317–328. https://doi.org/10.12989/was.2002.5.2_4.317.

Ishihara, T., Qi, Y.H., 2019. Numerical study of turbulent flow fields over steep terrains by using a modified delayed detached eddy simulations. Boundary-Layer Meteorol. 170, 45–68. https://doi.org/10.1007/s10546-018-0389-8.

Kim, H.G., Lee, C.M., Lim, H.C., Kyong, N.H., 1997. An experimental and numerical study on the flow over two-dimensional hills. J. Wind Eng. Ind. Aerod. 66 (1), 17–33. https://doi.org/10.1016/S0167-6105(97)00007-X.

Kim, J.J., Baik, J.J., Chun, H.Y., 2001. Two-dimensional numerical modeling of flow and dispersion in the presence of hill and buildings. J. Wind Eng. Ind. Aerod. 89 (10), 947–966. https://doi.org/10.1016/S0167-6105(01)00092-7.

Kobayashi, M.H., Pereira, J.C.F., Siqueira, M.B.B., 1994. Numerical study of the turbulent flow over and in a model forest on a 2D hill. J. Wind Eng. Ind. Aerod. 53 (3), 357–374. https://doi.org/10.1016/0167-6105(94)90091-4.

Kumar, V., Svensson, G., Holtslag, A.A.M., Meneveau, C., Parlange, M.B., 2010. Impact of surface flux formulations and geostrophic forcing on large-eddy simulations of diurnal atmospheric boundary layer flow. J. Appl. Metero. 49 (7), 1496–1516. https://doi.org/10.1175/2010JAMC2145.1.

Li, Y., Yan, L., He, X., 2024. Large eddy simulation study of 3D wind field in a complex mountainous area under different boundary conditions. J. Zhejiang Univ. (Agric. Life Sci.) 25, 541–556. https://doi.org/10.1631/jzus.A2300613.

Liu, L., Stevens, R.J., 2021. Effects of atmospheric stability on the performance of a wind turbine located behind a three-dimensional hill. Renew. Energy 175, 926–935. https://doi.org/10.1016/j.renene.2021.05.035.

Liu, Z., Hu, Y., Wang, W., 2019. Large eddy simulations of the flow fields over simplified hills with different roughness conditions, slopes, and hill shapes: a systematical study. Energies 12 (18), 3413. https://doi.org/10.3390/en12183413.

Liu, Z., Wang, W., Wang, Y., Ishihara, T., 2020. Large eddy simulations of slope effects on flow fields over isolated hills and ridges. J. Wind Eng. Ind. Aerod. 201, 104178. https://doi.org/10.1016/j.jweia.2020.104178.

Loureiro, J.B., Alho, A.T., Freire, A.P.S., 2008. The numerical computation of near-wall turbulent flow over a steep hill. J. Wind Eng. Ind. Aerod. 96 (5), 540–561. https://doi.org/10.1016/j.jweia.2008.01.011.

Monin, A., Obukhov, A.M., 1954. Basic laws of turbulent mixing in the surface layer of the atmosphere. Contrib. Geophys. Inst. Acad. Sci. USSR 151, e187. https://api.semanticscholar.org/CorpusID:198942767.

Narasimhan, G., Gayme, D.F., Meneveau, C., 2024. Analytical model coupling Ekman and surface layer structure in atmospheric boundary layer flows. Boundary-Layer Meteorol. 190 (4), 16. https://doi.org/10.1007/s10546-024-00859-9.

Neff, D.E., Meroney, R.N., 1998. Wind-tunnel modeling of hill and vegetation influence on wind power availability. J. Wind Eng. Ind. Aerod. 74, 335–343. https://doi.org/10.1016/S0167-6105(98)00030-0.

Pearse, J., Lindley, D., Stevenson, D., 1981. Wind flow over ridges in simulated atmospheric boundary layers. Boundary-Layer Meteorol. 21, 77–92. https://doi.org/10.1007/BF00119369.

Peng, M.S., Li, S.W., Chang, S.W., Williams, R.T., 1995. Flow over mountains: Coriolis force, transient troughs and three dimensionality. Q. J. R. Meteorol. Soc. 121 (523), 593–613. https://doi.org/10.1002/qj.49712152307.

Ross, A.N., Arnold, S., Vosper, S.B., Mobbs, S.D., Dixon, N., Robins, A.G., 2004. A comparison of wind-tunnel experiments and numerical simulations of neutral and stratified flow over a hill. Boundary-Layer Meteorol. 113, 427–459. https://doi.org/10.1007/s10546-004-0490-z.

Schumann, U., 1975. Subgrid scale model for finite difference simulations of turbulent flows in plane channels and annuli. J. Comput. Phys. 18 (4), 376–404. https://doi.org/10.1016/0021-9991(75)90093-5.

Song, Y., Yamaguchi, A., Ishihara, T., 2025. Prediction of vertical profiles of offshore wind considering the effects of atmospheric stratification. In: Proceedings of EERA Deep Wind 2025 Conference. https://www.sintef.no/globalassets/project/eera-deepwind-2025/posters/met-oceanyunpeng_song_prediction-of-vertical-profiles.pdf.

Takahashi, T., Ohtsu, T., Yassin, M.F., Kato, S., Murakami, S., 2002. Turbulence characteristics of wind over a hill with a rough surface. J. Wind Eng. Ind. Aerod. 90 (12–15), 1697–1706. https://doi.org/10.1016/S0167-6105(02)00280-5.

Uchida, T., Takakuwa, S., 2020. Numerical investigation of stable stratification effects on wind resource assessment in complex terrain. Energies 13 (24), 6638. https://doi.org/10.3390/en13246638.

Yamaguchi, A., Tavana, A., Ishihara, T., 2024. Assessment of wind over complex terrain considering the effects of topography, atmospheric stability and turbine wakes. Atmosphere 15 (6), 723. https://doi.org/10.3390/atmos15060723.

Yang, Q., Zhou, T., Yan, B., Liu, M., Van Phuc, P., Shu, Z., 2021. LES study of topographical effects of simplified 3D hills with different slopes on ABL flows considering terrain exposure conditions. J. Wind Eng. Ind. Aerod. 210, 104513. https://doi.org/10.1016/j.jweia.2020.104513.

Zhang, W., Markfort, C.D., Porté-Agel, F., 2023. Wind-tunnel experiments of turbulent wind fields over a two-dimensional (2D) steep hill: effects of the stable boundary layer. Boundary-Layer Meteorol. 1–21. https://doi.org/10.1007/s10546-023-00820-2.

Zhou, T., Ishihara, T., 2023. Numerical investigation of neutral atmospheric boundary layer flows over flat terrain and three-dimensional hills considering the effects of Coriolis force. J. Wind Eng. Ind. Aerod. 240, 105482. https://doi.org/10.1016/j.jweia.2023.105482.

Zhou, T., Ishihara, T., 2025. LES study of turbulent flow fields over a three-dimensional steep hill considering the effects of thermal stratification. Comput. Fluids 288, 106521. https://doi.org/10.1016/j.compfluid.2024.106521.

Zhou, T., Yan, B., Yang, Q., Hu, W., Chen, F., 2022. POD analysis of spatiotemporal characteristics of wake turbulence over hilly terrain and their relationship to hill slope, hill shape and inflow turbulence. J. Wind Eng. Ind. Aerod. 224, 104986. https://doi.org/10.1016/j.jweia.2022.104986.